

# Structure versus composition: a comparative study across scales

Yannicke Dauphin, <sup>\*ab</sup> Cedrik Lo, <sup>c</sup> Gergely Németh, <sup>d</sup>  
Christophe Sandt <sup>d</sup> and Jean-Pierre Cuij <sup>e</sup>

Received 19th January 2025, Accepted 3rd February 2025

DOI: 10.1039/d5fd00012b

Mollusk shells are composed of biominerals. While their mineral polymorphs are limited, their organic components number in the hundreds, if not thousands. Identifying these individual components is only the first step; understanding how they interact to form a shell remains an ongoing challenge. Infrared (IR) spectroscopy is a powerful technique for analyzing the structure and composition of these components while preserving their topographic relationships. This study employed three scales of observation and three samples: *Concholepas*, *Pinctada*, and cultivated pearls. Previously available data on their microstructure and compositions were utilized to explore potential correlations with results obtained from various techniques. IR analysis, being non-destructive, facilitates subsequent comparisons with other analytical methods such as Time-of-Flight Secondary Ion Mass Spectrometry (ToF-SIMS) and X-ray Absorption Near Edge Structure (XANES), thanks to the precise localization of IR data. The findings reveal that data from earlier non-IR analyses align with results from new IR techniques, including Diffuse Reflectance Infrared Fourier Transform (DRIFT), Optical Photothermal Infrared Spectroscopy (O-PTIR), and Scattering-Type Scanning Near-Field Optical Microscopy (sSNOM). This concordance validates the application of these new IR methods for studying biogenic calcium carbonate. Furthermore, the high spatial resolution of O-PTIR and sSNOM enables detailed visualization of structural and compositional features. For instance, the techniques reveal the intricate inner structure of three-month-old pearls, the distribution of proteins, lipids, and sulphated sugars in *Concholepas*, and the nanoscale differences in the arrangement of nacre and prisms in *Pinctada*.

<sup>a</sup>Institut de Systématique, Évolution, Biodiversité, UMR 7205, Muséum National d'Histoire Naturelle, 75005 Paris, France. E-mail: yannicke.dauphin@sorbonne-universite.fr

<sup>b</sup>Department of Biomaterials, Max-Planck Institute of Colloids and Interfaces, 14476 Potsdam, Germany

<sup>c</sup>Direction des Ressources Marines, BP 20, Papeete 98713, French Polynesia. E-mail: cedrik.lo@administration.gov.pf

<sup>d</sup>SMIS Beamline, Synchrotron SOLEIL, 91190 Saint Aubin, France. E-mail: gergely.nemeth@synchrotron-soleil.fr; christophe.sandt@synchrotron-soleil.fr

<sup>e</sup>Centre de Recherche sur la Paléodiversité et les Paléoenvironnements (CR2P), UMR 7207, Muséum National d'Histoire Naturelle, 75005 Paris, France. E-mail: jean-pierre.cuij@mnhn.fr



## Introduction

Biominerals, namely minerals produced by living organisms, are found across a wide range of taxa, both in modern and ancient times. They have existed for at least 550 My, while stromatolites have been known for approximately 3800 My. Fossil biominerals are used to reconstruct palaeoenvironments and evolutionary patterns, while certain modern taxa serve as food resources. The early exploration of biominerals, facilitated by the invention of the microscope, was pioneered by scientists like van Leeuwenhoek and Havers.<sup>1,2</sup> Concurrently, the studies of Réaumur on mollusk shells shed light on the distinct organic and mineral components that constitute biominerals.<sup>3</sup> Subsequent research has solidified the understanding that this dual composition is a fundamental characteristic of these materials.<sup>4-6</sup>

Given these characteristics, studying the composition of the mineralized parts of organisms is a challenge. A single shell consists of multiple layers, each with unique structure and composition. This makes even a sample of a few cubic millimeters a puzzle, and isolating the diverse components is often impractical. *In situ* observations are therefore essential for gaining a deeper understanding of these biogenic structures. Although WDS or EDS offer high sensitivity and spatial resolution, they predominantly focus on the inorganic components of biominerals. While early applications of IR spectroscopy were limited to polished or powdered samples, *in situ* FTIR microspectroscopic (MFTIR) analysis now reveals the relationship between structure and composition.<sup>7</sup> The diversity of mollusk shells, along with their abundance, has favoured their comparative study. X-ray diffraction studies have shown that they primarily consist of calcium carbonate in the form of aragonite, calcite, and vaterite. Since the pioneering work of Boggild,<sup>8</sup> it has been established that each species has a distinct structural and compositional profile.<sup>9,10</sup> Several infrared techniques are currently available for mapping the distribution of organic molecules and calcium carbonate phases.

In this paper, we explored three ranges of spatial resolution, spanning from micro- to nano-scale. To assess the efficacy of these techniques, we selected three mollusk shells, whose structures and compositions are partially understood. All samples were polished and then etched with a very weak acidic solution for 5 seconds to remove the polishing particles. *Concholepas*<sup>11,12</sup> was analysed at the microscale by Synchrotron-Radiation Diffuse Reflectance IR Fourier-Transform Spectroscopy (DRIFTS). We focused on the crossed lamellar layer. The initial growth stages of *Pinctada* pearls, characterized by irregular small structures, served as ideal candidates for submicron-scale analysis using super-resolved Optical-Photothermal Infrared Spectroscopy (OPTIR).<sup>13,14</sup> Finally, scattering-Scanning Nearfield Optical Microscopy (sSNOM) was employed to examine the nanoscale, specifically targeting the interface between the outer and inner shell layers of *Pinctada*.<sup>9,10</sup>

## Infrared data of $\text{CaCO}_3$ polymorph minerals

The groundbreaking study by Morse<sup>15</sup> compared the primary spectral features of  $\text{CaCO}_3$  samples and highlighted their differences. The introduction of commercial FTIR spectrometers in the 1960s, combined with the Cooley-Tukey algorithm

for fast Fourier transforms, spurred a surge in related publications. The distinctions between calcite and aragonite described by Morse were subsequently corroborated through systematic analyses of various  $\text{CaCO}_3$  species.<sup>16–19</sup> While many of these investigations focused on geological minerals, some extended to recent and fossil shells.

Currently, FTIR spectra of calcite and aragonite are defined by three major bands associated with the carbonate ion ( $\text{CO}_3^{2-}$ ): for calcite,  $\nu_3$  at  $1429\text{ cm}^{-1}$ , the  $\nu_2$  doublet at  $877\text{--}848\text{ cm}^{-1}$ , and  $\nu_4$  at  $713\text{ cm}^{-1}$ ; for aragonite,  $\nu_3$  at  $1471\text{ cm}^{-1}$ ,  $\nu_2$  doublets at either  $858\text{--}844\text{ cm}^{-1}$  or  $877\text{--}848\text{ cm}^{-1}$ , and  $\nu_4$  between  $713\text{--}700\text{ cm}^{-1}$ .<sup>20,21</sup> At this stage, based on the findings of Adler and Kerr,<sup>18</sup> White<sup>21</sup> concluded that “organically derived materials are spectroscopically indistinguishable”.

Nevertheless, biogenic minerals are not pure minerals; they contain organic components. The amide bands from proteins, amide I band appears between  $1600$  and  $1700\text{ cm}^{-1}$ , while the amide II band is found between  $1500$  and  $1600\text{ cm}^{-1}$ . Lipids have characteristic bands in the range of  $3000$  to  $2800\text{ cm}^{-1}$ , with strong peaks at  $2850\text{ cm}^{-1}$ ,  $2920\text{ cm}^{-1}$ , and  $2960\text{ cm}^{-1}$ . Sugars are identified by characteristic bands between  $1150\text{ cm}^{-1}$  and  $900\text{ cm}^{-1}$ . Thus, in organo-mineral assemblages, accurately assigning FTIR bands can be challenging due to the overlap of spectral bands.

## Fourier transform infrared spectroscopy at the micron scale

Typically, ribs and scales are present on the outer surface of the mollusk shell. When these reliefs are smooth, it is possible to remove contaminations due to sediment and/or epibionts. Another concern is the perforation due to sponges, fungi or Bryozoa. In this context, the shell of *Concholepas* serves as a case study, as its layer is covered by external organisms.

### The sample: shell of *Concholepas*

*Concholepas concholepas* (Bruguière 1789), a carnivorous gastropod, is native to the coasts of Chile and southern Peru. Most mollusk shells are predominantly made up of aragonitic crossed lamellar layers. *Concholepas* stands out due to its unique shell structure, making it an excellent candidate for *in situ* FTIR analysis to study millimeter-scale heterogeneities.

### Methods

DRIFT (Diffuse Reflectance Infrared Fourier Transform Spectroscopy) is a FTIR technique employed to analyze solid samples. In DRIFT, infrared radiation is directed at the sample. However, instead of passing through, the radiation is reflected off the surface. Only the diffusely scattered radiation from the sample is collected by a specialized mirror. This technique requires minimal sample preparation, making it suitable for analyzing powders and rough surfaces. Analysis can be relatively quick, and the sample remains intact after analysis.

Using the DRIFT technique on powdered samples, it was detected that the inner layer is composed of aragonite, while the outer layer is calcite.<sup>13,14</sup> Both layers contain a low organic matrix content. Despite the cleaning process, residual

incrustations from epibionts cannot be entirely excluded. Therefore, *in situ* FTIR analyses were subsequently conducted to establish the topographic correspondence between structure and composition.

Synchrotron infrared microscopy mapping was performed on the FTIR end-station of the ID21 beam line at the ESRF. This beam line is equipped with a Continuum IR microscope (Thermo Nicolet) coupled to a Nexus FTIR bench. The microscope operates in confocal mode, where the focusing Schwarzschild objective and the collection Schwarzschild objective have a magnification of  $32\times$  (NA = 0.65). Maps were scanned with steps of 4  $\mu\text{m}$  in both directions, with an aperture size of  $5 \times 5 \mu\text{m}^2$ . Spectra were collected in reflection mode, with a resolution of 8  $\text{cm}^{-1}$ . For each spectrum, 256 scans were accumulated in the wave-number range 4000–700  $\text{cm}^{-1}$ .

### Microstructures

The outer surface of the shell is characterized by prominent ribs, often encrusted with epibionts (Fig. 1a and b). Cross sections reveal two layers of varying thickness. The crossed lamellar layer has a thickness of about 120  $\mu\text{m}$ , while the prismatic layer measures approximately 2130  $\mu\text{m}$ . The inner layer, initially appearing to be composed of perpendicular “prismatic” units (Fig. 1c), upon closer examination, reveals a complex hierarchical structure (Fig. 1c and d). These “prisms” are, in fact, lamellae subdivided into several sub-order lamellae, forming a crossed lamellar layer. The outer layer, while described as “prismatic” lacks visible prisms in SEM images (Fig. 1e and f). To delve deeper into its organization, ultrathin sections (5–8  $\mu\text{m}$ ) were examined. Cross-nicols polarized light microscopy revealed elongated units with regular growth bands, suggesting a more intricate internal structure than previously recognized (Fig. 1g).

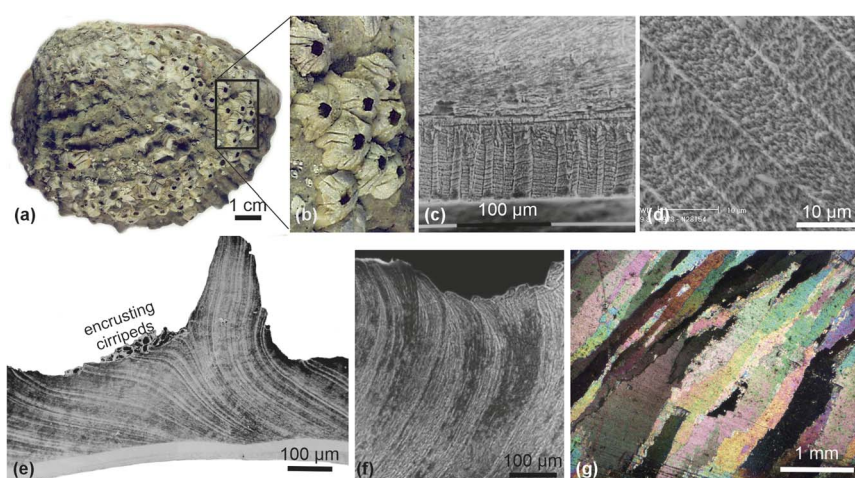


**Fig. 1** (a) Outer surface of the shell of *Concholepas*, encrusted with numerous epibiont arthropods. (b) Detail of (a) showing the epibionts. (c) Section of the shell showing the thin inner layer and the outer layer. (d) Detail of the structure of the inner crossed lamellar layer. (e) Section showing the growth layers of the “prismatic” outer layer. Note: encrusting epibionts visible on the outer surface of the shell. (f) Detail of the growth layers in the outer prismatic layer. (g) Thin section showing the irregular pattern in the outer prismatic layer.



## Composition

DRIFT spectra of the powdered outer layer indicate a calcitic mineralogy, characterized by the  $\nu_2$  doublet at  $877\text{--}848\text{ cm}^{-1}$ ,  $\nu_1$  at  $1013\text{ cm}^{-1}$  and  $\nu_4$  at  $713\text{ cm}^{-1}$ . The  $\nu_3$  band is subdivided: 1457, 1445 and  $1436\text{ cm}^{-1}$  (Fig. 2). Additionally, bands usually associated with calcite such as those at 1176 and  $1084\text{ cm}^{-1}$  are present. Several bands may be attributed to the organic matrix: the  $3274\text{ cm}^{-1}$  band for amide A,  $1685\text{--}1653\text{--}1636\text{ cm}^{-1}$  bands for amide I. The inner layer exhibits an aragonitic composition, with a subdivided  $\nu_3$  band at 1492 and  $1458\text{ cm}^{-1}$ , a single  $\nu_2$  band at  $863\text{ cm}^{-1}$ , and a  $\nu_1$  band at  $1083\text{ cm}^{-1}$ . The amide A band appears at  $3310\text{ cm}^{-1}$ , while the amide I region shows two bands at 1654 and  $1636\text{ cm}^{-1}$ . Both calcitic and aragonitic layers included organic matrix. To estimate the organic/mineral ratio from FTIR spectra, two ratios were used: amide I/ $860$  and amide A/ $860$  for aragonitic layers.<sup>22</sup> In crossed lamellar layers, these ratios are 0.14 and 0.08, respectively. For calcitic layers, the  $878\text{ cm}^{-1}$  band is used, and the corresponding ratios are 0.23 and 0.07. The provided FWHM values (full width at half maximum) indicate that both aragonite and calcite exhibit similar levels of crystallinity. The slight difference in FWHM (180 for aragonite and 184.5 for calcite) suggests that calcite might have slightly lower crystallinity compared to aragonite. However, this difference is relatively small and might not be significant.

Polished section maps clearly differentiate aragonitic crossed lamellar and calcitic prismatic layers (Fig. 3a), with a mineralogical transition at  $1493\text{ cm}^{-1}$  (Fig. 3a and b). The crossed lamellar layer displays a fine structure of first-order lamellae, while the outer layer appears homogeneous. A map at  $1540\text{ cm}^{-1}$  reveals similar amide II content in both layers (Fig. 3c). The crossed lamellar layer pattern resembles that at  $1493\text{ cm}^{-1}$ , but with colour variations within first-order lamellae suggesting the presence of second-order lamellae. The inner layering of the prismatic layer is more apparent at  $1540\text{ cm}^{-1}$ . A map at  $1608\text{ cm}^{-1}$  less clearly defines the inner structures of both layers, with only subtle intensity differences (Fig. 3d).

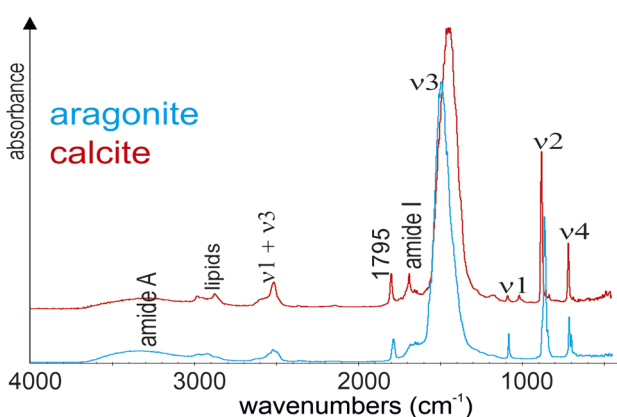


Fig. 2 DRIFTS spectra of powdered layers of the shell of *Concholepas*. The inner crossed lamellar layer is aragonite, the prismatic layer is calcite. Despite the moderate heating process ( $40\text{ }^\circ\text{C}$ ) the presence of water associated with organic matrices cannot be excluded. A very weak shoulder at  $1450\text{ cm}^{-1}$ , not visible here, is located in the slope of the  $\nu_3$  band.



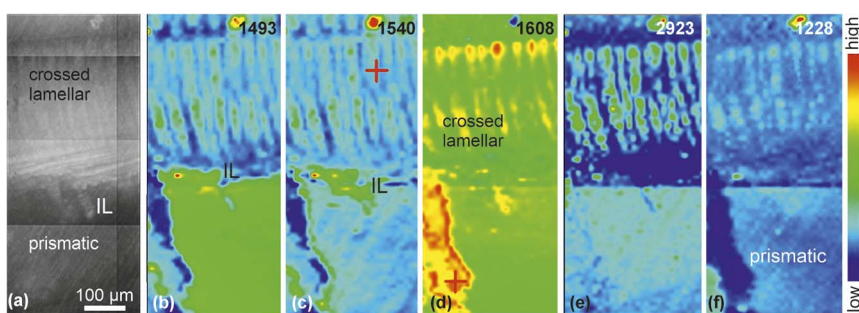


Fig. 3 (a) Polished section showing the localization of maps in the shell of *Concholepas*. IL: intermediate layer; prismatic: prismatic layer; (b) map at  $1493\text{ cm}^{-1}$  showing the crossed lamellar pattern of the aragonitic layer. The intermediate layer (IL) is not evidenced. (c) Map at  $1540\text{ cm}^{-1}$  for amide II showing faint growth layers in the calcitic layer. (d) Map at  $1608\text{ cm}^{-1}$  showing that both layers have a similar content in organics. (e) Map at  $2923\text{ cm}^{-1}$  showing the crossed lamellar pattern and the difference in lipid contents. (f) Amide III and/or sulphated GAGS map showing the inner structure of the inner and outer layers.

The intermediate layer (IL), and the beginning and end of the crossed lamellar layer at  $2923\text{ cm}^{-1}$  (Fig. 3e), indicate a variable lipid content. Amide III and/or  $\text{SO}_3$  in sulphated GAGS<sup>23</sup> distribution map is shown in the  $1228\text{ cm}^{-1}$  map (Fig. 3f).

### Comments

DRIFTS analyses are fast, easy to perform, and useful for selecting wavenumbers and mapping locations. Mapping techniques, such as SEM and IR, provided complementary insights for sample characterization. While SEM offers higher spatial resolution than FTIR, combining both techniques allows the estimation of the interplay between mineralogy, structure, and composition in specific zones. Maps clearly show the inner structure of units and the transition between the two main layers, which varies depending on the wavenumber. FTIR spectroscopy on powdered shell layers reveals a correlation between the wavenumber and the content of Mg and Sr in calcite and aragonite.<sup>24,25</sup> The observed wavenumbers in the shell layers of *Concholepas* are consistent with low Mg content in calcite and low Sr content in aragonite.<sup>13</sup> Additionally, FTIR spectra of the powdered shell layers reveal the presence of organic components. However, spectral overlap can limit the extent of interpretation. Another problem is the large variety of organic components. For example, more than 900 proteins were identified as constituents of the chicken eggshell matrix.<sup>26</sup> No data are available for sugars and lipids. Thus, two maps obtained at a given wavenumber will likely be different if a slight polishing was done between the two acquisitions. Sulphated polysaccharides have been identified in *Concholepas* using XANES analyses.<sup>27</sup> However, with the current data, we cannot quantify their relative proportions.

## Optical photothermal infrared (O-PTIR) spectroscopy at the submicron scale

Cultivated pearls are created through a grafting process. In French Polynesia, this process, inspired by Mikimoto and Mise, involves inserting a small piece of



mantle tissue (the graft) into the gonad of a pearl oyster, along with a spherical nucleus. The graft then secretes layers of black nacre, gradually covering the nucleus. After approximately two years, the nucleus is encased in a thick nacreous layer, and the pearl is harvested. However, this ideal growth is rarely achieved.<sup>28-31</sup>

### The sample: Polynesian cultivated pearls from *Pinctada margaritifera*

The quality of a pearl is determined by its shape (ideally a perfect sphere) and surface quality of its outer layer. According to Charpentier *et al.*,<sup>32</sup> neolithic "fishermen selected pearls according to their shape, *i.e.* they preferred those that were more or less spherical". However, the inner structure and composition of the pearl layer remain relatively poorly understood. Rare sections of cultivated pearls have revealed that the theoretical pattern of nucleus and nacre may not always hold true.<sup>28-31</sup> Additionally, tomography studies have confirmed that the pearl layer often deviates from the expected theoretical model.<sup>33,34</sup> While tomography now allows us to visualize the inner structure of a pearl, it cannot directly determine its composition. To bridge this gap, we employ *in situ* analysis to decipher the intricate relationship between structure and composition at a microscopic level.

### Methods

O-PTIR (Optical-Photothermal Infrared Radiometry) is a non-contact, non-destructive technique that enables the analysis of shell composition at the nanoscale, offering submicron spatial resolution of 450 nm. It operates by directing two lasers onto the sample: an infrared laser that heats the material and a visible laser (typically at 532 nm) that measures the resulting thermal response. When the infrared laser strikes the material, it causes a slight expansion due to the heat. The 532 nm laser detects this expansion by measuring changes in the optical properties of the surface, allowing the creation of an image that reflects the infrared absorption characteristics of the sample.<sup>35-37</sup>

OPTIR was performed at the SMIS beamline using a mIRage microscope (Photothermal Spectroscopy Corporation, Santa Barbara, CA, USA) controlled by the PTIR Studio 4.6 software. The infrared pump laser was a four-stage MIRCat pulsed, tunable Quantum Cascade Laser (Daylight Solutions, San Diego, CA, USA), scanning in the ranges 920 to 1800 and 2700 to 3026 cm<sup>-1</sup> and pulsed at 100 kHz. The probe laser was a Continuous Wave 532 nm laser and its photothermally induced modulation was recorded with an Avalanche Photo Diode detector (APD) detector. Both lasers were focused on the sample through a 40 $\times$ /0.78NA Schwarzschild objective (Pike Technologies, Madison, WI, USA) and data was collected in reflection/copropagation mode. A background spectrum was collected on an IR-reflective ITO layered low-emissivity glass slide (Kevley Chesterland OH, USA) with 25 coadded scans.

### Microstructures

Although the nucleus is typically spherical, irregularities in pearl shape likely result from fluctuations in the secretion process following grafting (Fig. 4a). Regardless of the overall shape, a layer of organic material, varying in thickness, consistently separates the nucleus from the initial pearl deposits (Fig. 4b). The subsequent pearl layer comprises concentric sublayers of poorly defined prisms,

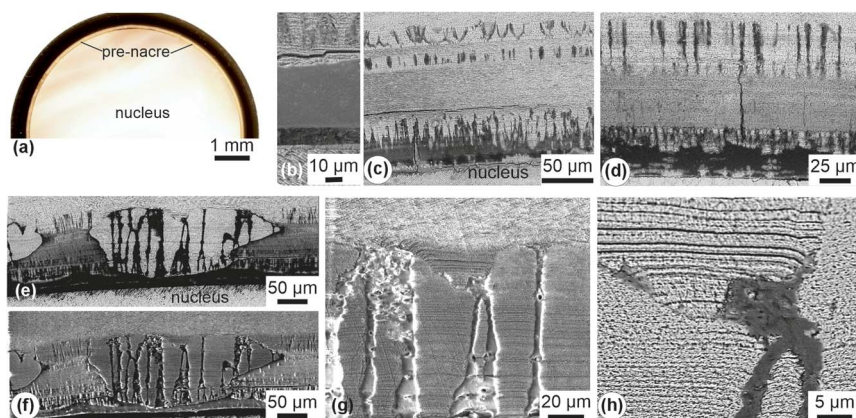


**Fig. 4** (a) Section revealing the nucleus and the 3-month-old pearl layer. (b) Section illustrating the initial deposits: the nucleus, a lacuna, and a subsequent thick organic layer. The structure of the first mineralized layer is irregular. (c) Section of the first layer, displaying an abundant organic matrix (black), followed by progressively forming mineralized pseudo-prisms. Pre-nacre layers alternate with pseudo-prisms. SEM BSE image. (d) A similar pattern observed in another pearl. SEM BSE image. (e and f) Section showcasing the irregular pattern of calcitic and aragonitic patches, 3-month-old pearl. (e) SEM BSE image, (f) SEM SE image. (g) A detailed view of the interprismatic organic membranes. (h) Growth layers within the pseudo-prisms are not discernible in the organic membranes.

also known as pseudo-prisms. Notably, the thickness, diameter, and shape of these pseudo-prisms vary within a given growth layer (Fig. 4c and d). Prior to the nacre layer, thin lamellar layers are deposited, but they lack the polygonal tablets characteristic of true nacre. The recovery of the graft and subsequent nacre formation is unstable, as evidenced by irregular patches of calcite and aragonite (Fig. 4e and f). Backscattered electron (BSE) scanning electron microscope (SEM) images reveal that these deposits are rich in organic components (Fig. 4e). Growth layers are visible in both the calcite and aragonite structures (Fig. 4f-h). When present, the outermost layer, black nacre, is clearly discernible (Fig. 4a). The thickness of these structures varies within individual pearls, and their size, shape, and number vary between different pearls.<sup>26,30</sup> Furthermore, only *in situ* analyses can provide a comprehensive understanding of these structural arrangements, making mapping essential.

## Composition

The irregular thin pearl layer structures make powdered samples unsuitable for precise compositional analysis. To circumvent this limitation, we employed infrared spectroscopy in various pearl specimens. Nevertheless, the inherent spatial resolution limitations of FTIR mapping hindered a detailed analysis. To address this, we utilized the O-PTIR system to enable a more precise investigation of the sample. While previous analyses have demonstrated the coexistence of calcite and aragonite during graft recovery, leading to mineralized deposits, the prevalence of this pattern is still unknown. Moreover, data about the organic components are still scarce.

SEM-BSE images illustrate differences in the quantity and localization of organic components (Fig. 4). Polished sections reveal pseudo-prisms as a series of



narrow, W-shaped, black structures with organic-like components. This observation aligns well with SEM and O-PTIR imaging results. The selected zone is the first deposits on the nucleus, visible in Fig. 4e-h and 5a, b. The nucleus is not included, but pseudo-prisms and their envelopes are visible. Based on knowledge of the pearl layer composition, two wavenumbers (1082 and 1510  $\text{cm}^{-1}$ ) were selected as indicative of aragonite (Fig. 5c and d). Maps were generated at 1238 and 1654  $\text{cm}^{-1}$  (Fig. 5e and f) attributed to cartography proteins, while a map at 2928  $\text{cm}^{-1}$  was attributed to lipids (Fig. 5h). Comparing SEM-BSE images of the pearl layer with IR maps confirms the organic nature of the layer situated between the nucleus and the initial mineralized deposits. The majority of the maps reveal pseudo-prisms, locally separated by organic envelopes with varying protein and lipid content. Distribution maps corroborate that not all prisms are embedded in organic envelopes, a pattern consistent with SEM images (Fig. 4). The discontinuity of the inter-prismatic membranes (ipm) is evident in maps at 1238 and 1654  $\text{cm}^{-1}$ , wavenumbers characteristic of proteins. Furthermore, maps at 1654 and 1082  $\text{cm}^{-1}$  suggest a subtle layering pattern within the prisms. Enhancing the contrast of Fig. 5e highlights the rhythmic nature of the growth layers in

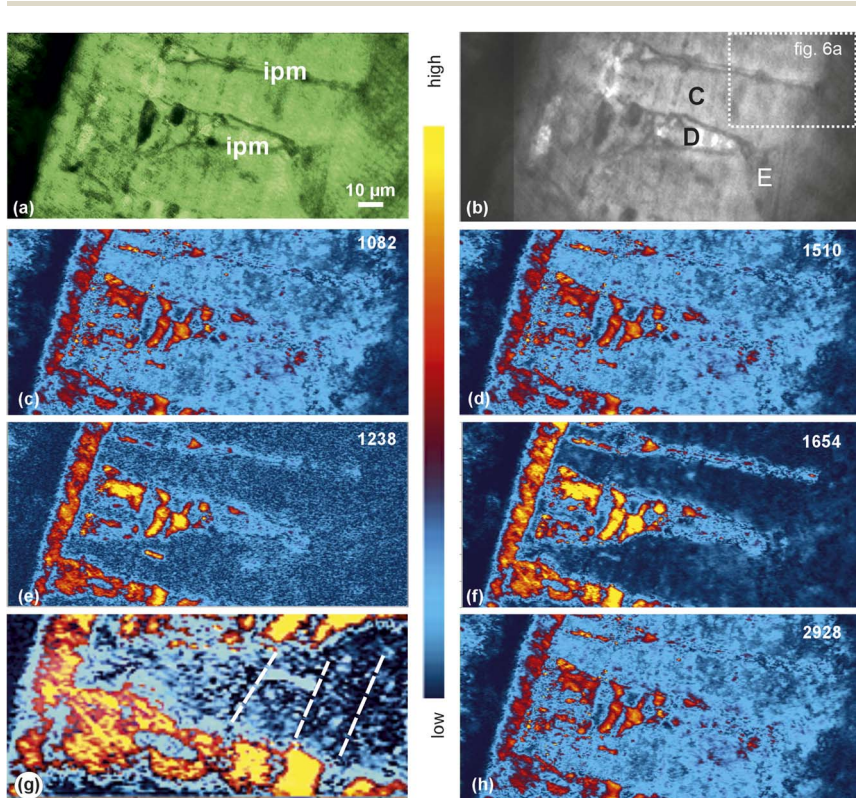


**Fig. 5** (a and b) Cross-sectional views of the early stages of pearl layer formation, with the nucleus positioned to the left. ipm: inter-prismatic membrane; C-E: localisation of spectra acquisition in different prismatic units. (c-f) Distribution maps for aragonite (1082, 1510  $\text{cm}^{-1}$ ) and proteins (1238, 1654  $\text{cm}^{-1}$ ). (g) Magnified view of (e), emphasizing the discontinuous nature of the inter-pseudo-prismatic organic matrix. Growth lines are suggested by yellow shapes and white dashed lines. (h) Map of lipids (2928  $\text{cm}^{-1}$ ).



envelopes and within the pseudo-prisms (Fig. 5g, white dashed lines). A comparison of the distribution maps in Fig. 5 reveals consistent patterns between  $1084\text{ cm}^{-1}$  and  $1510\text{ cm}^{-1}$ , suggesting the presence of aragonite, and between  $1238\text{ cm}^{-1}$  and  $1654\text{ cm}^{-1}$ , for proteins.

Extracting spectra from the maps reveals differences between zones smaller than  $10\text{ }\mu\text{m}$ , enabling precise correlation of structures and compositions with their locations. While subtle colour variations may be less distinct on the map, spectral differences within small zones are readily apparent. Spectra more clearly display compositional heterogeneity (Fig. 6). Fig. 6a demonstrates the dual organic and mineral composition. Both black and white zones exhibit carbonate bands at approximately  $1450\text{ cm}^{-1}$ , but only one displays the aragonitic band at  $1084\text{ cm}^{-1}$  (Fig. 6a, \*). Organic bands (at approximately  $1660\text{ cm}^{-1}$  for amide I and  $1540\text{ cm}^{-1}$  for amide II) dominate spectra obtained from the organic membrane (Fig. 6a and b). Despite the small size of the zone D (Fig. 5b), significant variations occur within zone D (Fig. 6b and c). Mineral components dominate zone E with: a small, regular band at  $1082\text{--}1084\text{ cm}^{-1}$  attributed to aragonite (Fig. 6d), although a weak shoulder at  $1650\text{ cm}^{-1}$  suggests the presence of some proteins.

This investigation also examines the interface between aragonite and calcite deposits. Growth layers are apparent in both zones (Fig. 7a and b), though their potential continuity is obscured by the abundant organic matrix. These layers exhibit variable thickness, ranging from 1 to  $3\text{ }\mu\text{m}$ , within each pseudo-prism. Within the thickest growth layers, a substructure with small, needle-like units is evident, oriented perpendicular to the overall growth layering pattern (Fig. 7c).

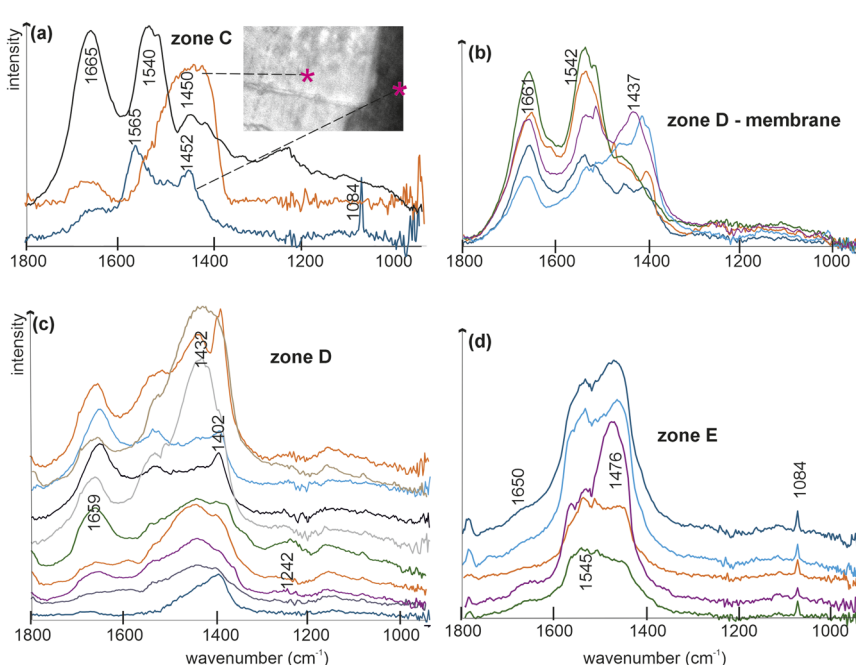


Fig. 6 Spectra extracted from small zones identified in Fig. 5a and b showing the diversity of the organo–mineral assemblages.



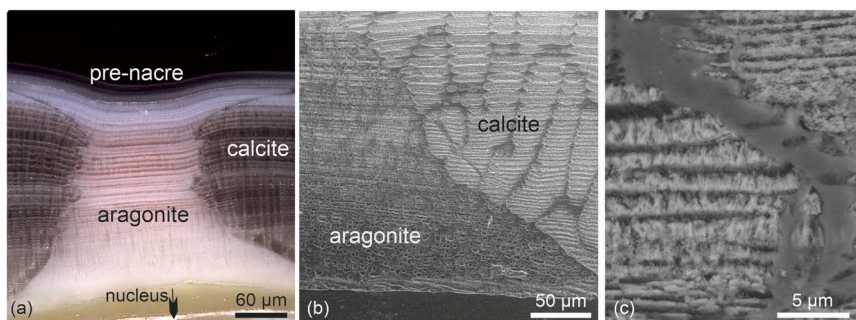


Fig. 7 Contact region between calcite and aragonite. (a) Polished section showing deposits from the nucleus to the layered pre-nacre structure. (b) SEM image showing the layered pattern on calcite. (c) Detail of the structure in growth layers and organic membrane between calcite and aragonite.

However, evidence for thin organic membranes between the growth layers, as observed in nacre, is not found.

The difference between the calcite and aragonite regions is evident in O-PTIR maps (Fig. 8). Maps at 1082 and 1510  $\text{cm}^{-1}$ , indicative of aragonite, do not exhibit perfect correlation (Fig. 8c and d). It must be remembered that these deposits are unstable in structure, and probably in composition. Wavenumbers and chemical elements are correlated.<sup>24,25</sup> Growth layers are more prominent in the calcitic region for maps at 1510, 1450, and 1656  $\text{cm}^{-1}$  (Fig. 8d-h). Conversely, in aragonitic region, very thin lines (<1–2  $\mu\text{m}$ ) are arranged in

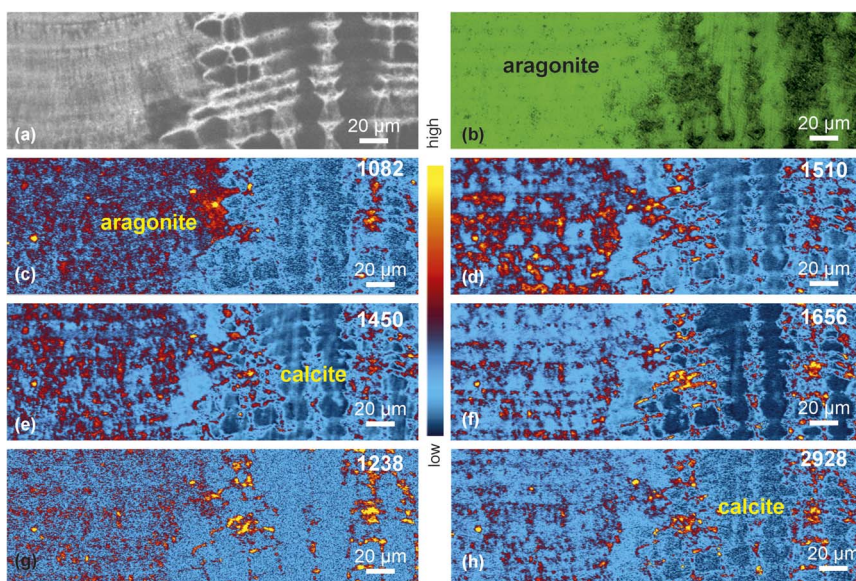


Fig. 8 Structure and composition at a microscale showing the difference between aragonite region and pseudo-prismatic calcite. The organic inter-prismatic envelopes and the intra-pseudo-prisms growth layers are well visible in both aragonite and calcite.



a layered pattern for maps at 1656 and 2928  $\text{cm}^{-1}$  (Fig. 8f and h). Organic inter-pseudoprismatic membranes are detected in all maps, albeit with varying intensities. Generally, these membranes are thicker than those within the pseudo-prisms. Although inter- and intra-pseudo prismatic membranes are present, the arrangement of aragonite does not resemble that of nacre, and the prisms differ from those found in the shell of *Pinctada*. At this stage (3-month-old pearl), calcareous deposits completely covered the nucleus, but their structure and mineralogy remained unstable.

## Comments

O-PTIR analyses on bone and non-biological samples have demonstrated high spatial resolution,<sup>35</sup> enabling the detection of minute features, previously overlooked. This high spatial resolution allows for the precise mapping of the distribution of the organic components.<sup>36,37</sup> O-PTIR imaging is now feasible, enabling correlation with SEM images at comparable magnifications. Not only are the thick organic inter-pseudo-prismatic membranes visible, but also thin organic layers are detected, demonstrating their discontinuous nature, and mirroring the growth layers. Furthermore, the inner heterogeneous structure of the pseudo-prisms is revealed.

Beyond the visual quality of the images, it is possible to quantify parameters such as crystallinity and organic-to-mineral ratio within distinct zones. This enables the calculation of variations in a given parameter within a specific zone using surface areas or peak intensities. For example, colocalization analysis of maps for aragonite, proteins, and lipids (Table 1) in the sample shown in Fig. 5, revealed the highest correlation between lipids and proteins ( $r = 0.90$ ). The weakest correlation ( $r = 0.62$ ) was observed between aragonite maps. This suggests that the 1510  $\text{cm}^{-1}$  band likely also encompasses contributions from organic components rich in amide II. While O-PTIR offers many advantages, it may not be ideal for analyzing  $\text{CaCO}_3$ . The 1082  $\text{cm}^{-1}$  band is typically assigned to aragonite, but identifying calcite using O-PTIR can be challenging.<sup>35,36</sup> However, bands observed around 1420–1450  $\text{cm}^{-1}$  are characteristic of carbonates. In the context of mollusk shells and coral skeletons, these bands are likely associated with calcite, similar to their interpretation in FTIR analysis.

Table 1 Pearson coefficient correlations for co-localisation of images shown in Fig. 5

	Aragonite 1082	Proteins 1238	Aragonite 1510	Proteins 1656	Lipids 2928
<b>1082</b>					
<b>1238</b>	0.66				
<b>1510</b>	0.62	0.67			
<b>1656</b>	0.78	0.71	0.62		
<b>2928</b>	0.81	0.75	0.69	0.90	



# Nanoscale scattering-type scanning near-field optical microscopy (s-SNOM)

Nanoscale studies on biogenic biominerals remain limited. NanoFTIR was used to study the fibrous calcite layer and nacreous aragonite in the *Mytilus* shell.<sup>37</sup> Layers were distinguished based on their spectral characteristics: aragonite exhibits a peak at  $855\text{ cm}^{-1}$ , while calcite displays a peak at  $872\text{ cm}^{-1}$ . However, data regarding the presence of organic matrices was not provided. Historically, the low abundance of organic components has hindered research on mollusk shells and coral skeletons.

## The sample: transition from prisms to nacre in *Pinctada*

One of the best-known shells is that of the pearl oyster, *Pinctada*, due to its commercial importance.<sup>38–45</sup> *P. margaritifera* holds a unique status: like other *Pinctada* species, it possesses a black prismatic layer and a white nacre. However, in French Polynesia, the nacre is initially black, gradually turning gray. Thus the Polynesian black lip pearl oyster is considered to be a subspecies: *P. margaritifera* (Linné, 1758) var *cumingi*. The intricate and diminutive nature of these elements (membrane, prisms, nacre) presents a significant challenge for detailed characterization, resulting in a limited understanding. We use nanoscale infrared (sSNOM) to elucidate the calcite–aragonite separation.

## Methods

The resolution of the optical MFTIR techniques is limited by the wavelength of the probing light waves. By employing green lasers, the O-PTIR technique significantly enhances spatial resolution, but it is still limited by the probe laser wavelength.

Scattering-type scanning near-field optical microscopy (s-SNOM) can be used to achieve the ultimate spatial resolution with chemical sensitivity. sSNOM is an AFM-based probing method where the AFM tip is illuminated by focused infrared radiations. In sSNOM, the metal-coated AFM tip acts like an antenna, concentrating the light into an optical near-field in the vicinity of the apex of the tip, by a factor of up to  $10^5$  times. The effective size of this concentrated light field is on the order of the AFM tip, which is 20–30 nm. This concentrated electromagnetic field interacts with the sample that can absorb and scatter the IR radiation, exciting molecular vibration modes in the sample. The back scattered light is collected by the microscope optic and focused in an MCT detector. To separate the near-field scattering from the background, the AFM works in tapping mode and an interferometric detection scheme is used to measure the amplitude and the phase of the scattered light.<sup>35,46,47</sup> In a single measurement the method provides the AFM topography, the optical amplitude and optical phase images (sSNOM image). The optical phase image can be interpreted as an IR absorption image. With a broadband IR source such as the synchrotron source, the optical phase can be transformed into a nanoFTIR spectrum thanks to the interferometric detection setup.

We operated a commercial sSNOM instrument (IR-neaSCOPE+, Attocube GmbH, Haar, Germany) at the SMIS beamline of Synchrotron SOLEIL. To identify

the specific components of the shell, we used the broadband synchrotron light to collect point spectra in different locations identified by the visible and AFM images. When the specific absorption bands are determined and assigned to a component, we swap the light source to a tunable quantum cascade laser (MIRcat-QC, DRS Daylight Solution, San Diego, CA, USA). By tuning the laser to its specific absorption frequency we can visualize the spatial distribution of the chosen component.

## Microstructure

The *Pinctada* shell consists of two primary layers: an outer prismatic calcitic layer and an inner aragonitic nacreous layer (Fig. 9a). These layers are approximately

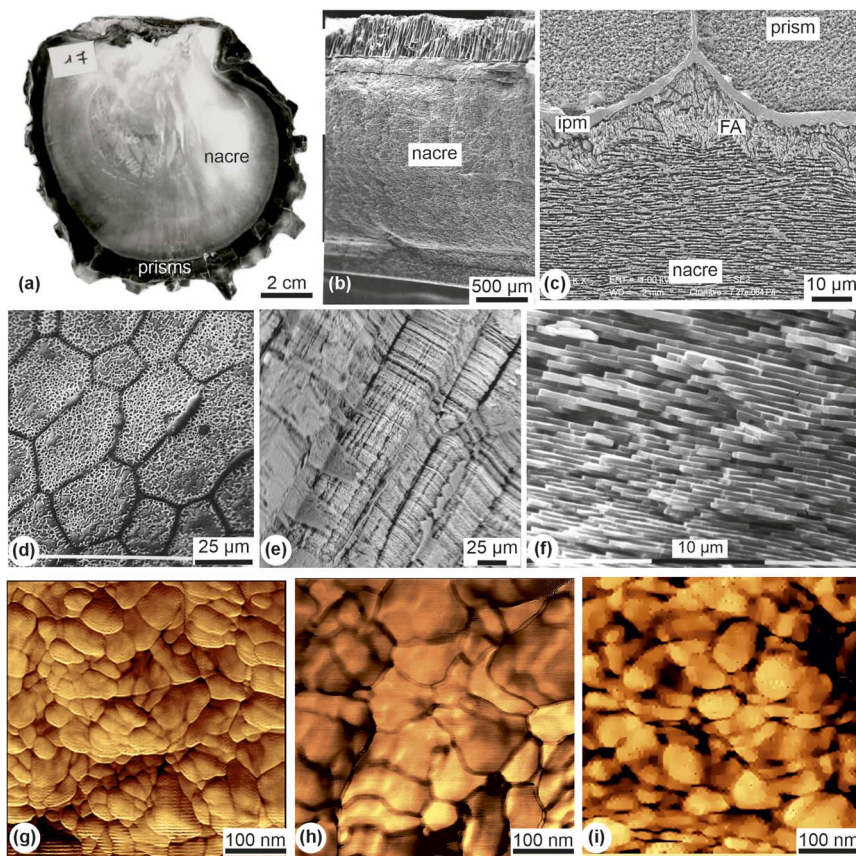


**Fig. 9** Microstructure of the shell of the pearl oyster, *Pinctada margaritifera*. (a) Inner surface of a valve showing the main mineralized layers: nacre and prisms. (b) Vertical section showing the thick nacreous layer and the thin outer prisms. (c) Vertical section of the shell showing the interprismatic organic layer, the prisms, the fibrous aragonite and the nacre. (d) Polished, etched and fixed section showing the intraprismatic and interprismatic organic components. (e) Longitudinal section showing the thin growth layers and the remains of the organic envelopes after being etched by an enzymatic solution. (f) Fracture showing the nacreous tablets. (g-i) AFM phase images showing the granules in the nacreous layer (g and h) and the prisms (i). FA: fibrous aragonite, ipm inter-prismatic membrane.



400  $\mu\text{m}$  and 2 mm thick, respectively (Fig. 9b). Research predominantly focuses on the nacre, as its quality significantly influences pearl value. Separating these two main layers is an irregular and thin fibrous aragonitic layer (Fig. 9c). Cross-sectional fractures reveal that the inner surface of the prisms is V-shaped (Fig. 9c). Transverse sections show that the shape of the prism is polygonal (Fig. 9d). A fixation-decalcification process of the prisms preserves the organic components, resulting in a dense network-like appearance of the surface (Fig. 9d).<sup>40,48</sup> While the shape and distribution of this network may be an artifact of the preparation process, it indicates an abundant intraprismatic matrix. Enzymatic etching of a longitudinal section reveals the organic inter-prismatic membranes and growth layers within the prisms (Fig. 9e). The nacreous layer exhibits the typical structure found in *Bivalvia* shells (Fig. 9f). Nacreous tablets are organized into “sheets” separated by interlamellar organic membranes, and within a sheet, tablets are separated by intercrystalline organic membranes. Despite their mineralogical and microstructural differences, the fundamental nanoscale units of nacre and prisms share a similar structure (Fig. 9g–i).<sup>49,50</sup> These units consist of rounded granules enveloped by a thin organic-ACC (Amorphous Calcium Carbonate) cortex. Notably, SNOM and classical AFM images exhibit a strong resemblance (Fig. 9g–i).

## Composition

The *P. margaritifera* shell is as follows: a calcitic prismatic layer, an aragonitic fibrous layer and a nacreous layer. A membrane separates the calcite and aragonite layers.

The first region investigated using high-resolution SNOM imaging and nano-FTIR spectroscopy was the transition zone between the outer prismatic and the inner fibrous and nacreous layers, resembling the region illustrated in Fig. 9c. The AFM image of the selected area is presented in Fig. 10c. The lower portion of the zone (1 in Fig. 10c) is presumed to be the fibrous/nacreous structure, while the upper half (labeled 3 and 4) is believed to be prismatic. These regions are separated by a thin (0.1–1  $\mu\text{m}$ ) layer. To identify the distinct components, we utilized synchrotron-based nanoFTIR spectroscopy to measure the local infrared response of different areas within the four points marked in the AFM image. Fig. 10d displays the measured phase spectra. As previously mentioned, phase spectra can be interpreted as nanoscale absorption spectra. However, it is crucial to note that the spectral location of the peaks can differ significantly from conventional and OPTIR spectra. The spectra reveal three primary components, as anticipated: calcitic regions (Points 3 and 4) with two prominent bands at 880  $\text{cm}^{-1}$  and 1488  $\text{cm}^{-1}$ , the aragonite region (Point 1) with main peaks at 863  $\text{cm}^{-1}$  and 1528  $\text{cm}^{-1}$ , and the organic layer (Point 2) with its amide band at 1650  $\text{cm}^{-1}$ .

After determining the correct nanoscale absorption wavelengths, we employed a tunable single-frequency laser to map the distribution of the corresponding components. Fig. 10a displays the near-field phase image of the same region at 1464  $\text{cm}^{-1}$ . This frequency was utilized to image both components within a single image. As observed in the spectra, the highest phase values correspond to calcite, the mid-range values to aragonite, and the near-zero values to the organic layer. To better visualize the organic component, we acquired an additional map specifically targeting the amide band of proteins at 1650  $\text{cm}^{-1}$ , presented in Fig. 10b.



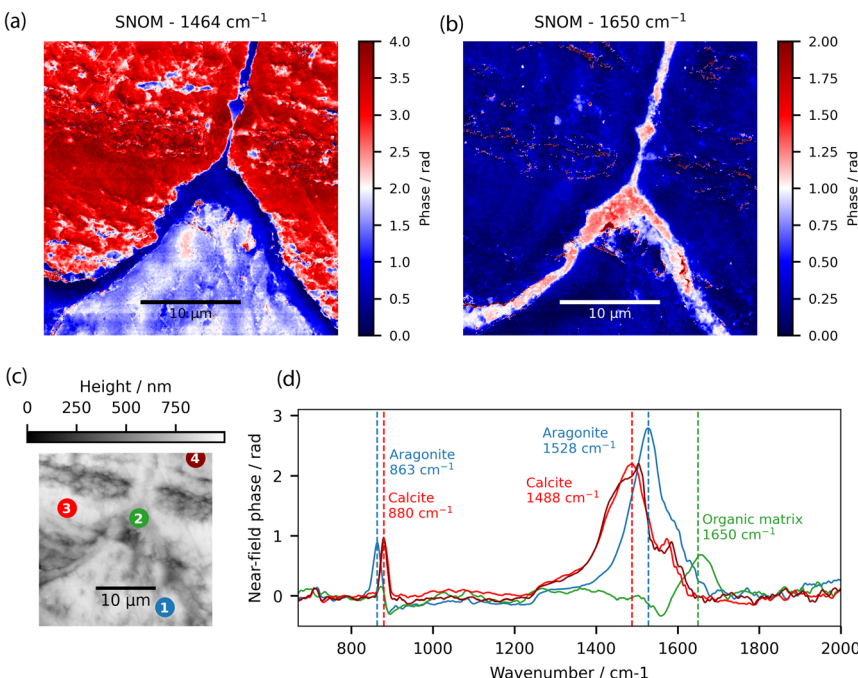


**Fig. 10** Nanoscale characterization of the transition zone between the nacreous and prismatic layers. (a and b) Single-wavelength near-field phase images specific to calcite ( $1464\text{ cm}^{-1}$ ) and amide/organic ( $1650\text{ cm}^{-1}$ ) nanoFTIR bands. (c) AFM topography image of the area of interest. The coloured spots mark the points of nanoFTIR measurements. (d) The resulting spectra of the different locations. The colours of the lines correspond to the colours of the points.

Following the study of the transition zone, we also analyzed the structure deep inside the prismatic or nacreous regions. Fig. 11 renders the results in the nacreous side of the shell. It shows a typical spot deep inside the nacre. Fig. 11a–c present the AFM topography, and the near-field amplitude and phase images, respectively, at  $1650\text{ cm}^{-1}$ . As the figure proves, the nacreous layer has an alternating pattern of aragonite and organic interlamellar layers. The thickness of the nacreous tablets is smaller than  $1\text{ }\mu\text{m}$ . Less visible are the intercrystalline organic layers, perpendicular to the interlamellar layers (Fig. 11c). To confirm that the contrast in the phase images really comes from the organic compound, we measured nanoFTIR spectra at random points. In several spots we can note a decreased aragonite peak with the amide peak arising at  $1650\text{ cm}^{-1}$ .

We followed the same procedure for the study of the prismatic part as that of the nacreous region. The results are represented by Fig. 12. As evident from the near-field phase (Fig. 12c), this region is not as organized as the nacreous and contains organic constituents randomly around the granular features. However, the near-field phase shows elevated contrast in several larger spots which might be attributed to other organic compounds but there is no significant sign in the nanoFTIR spectra (Fig. 12e). The spectra also confirm the lack of significant amide peaks, with only a slight variation in the calcite bands. This variation could



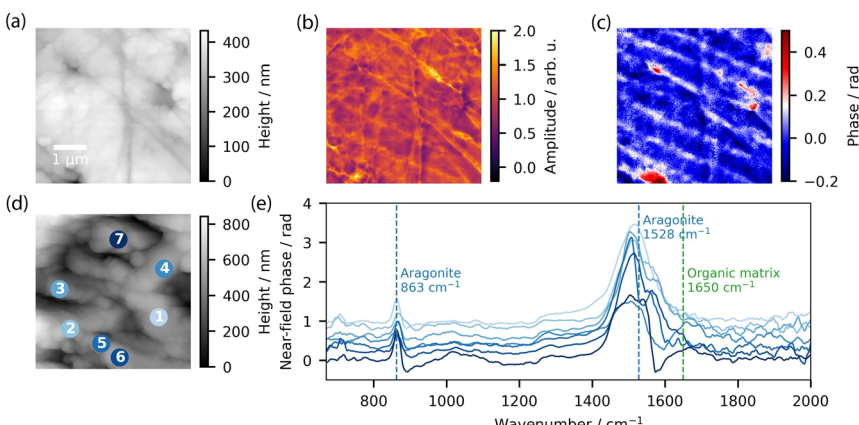


**Fig. 11** Nanoscale composition of nacreous layer. (a) AFM topography, (b and c) near-field amplitude and phase images at the absorption band of the organic components ( $1650\text{ cm}^{-1}$ ). Both images show an alternating structure of organic and aragonite layers. (d) and (e) AFM topography and nanoFTIR spectra. The spectra taken at different points show signatures of both aragonite and organic compounds.

be associated with the local changes in crystallinity and orientation since calcite is a highly anisotropic material.

## Comments

The mineralogy of *P. margaritifera* shells is well known, but our understanding of their organic composition remains limited. Notably, topographic relationships between mineral and organic components at submicron and nanoscales are not yet fully established. Our current knowledge of the organic components primarily

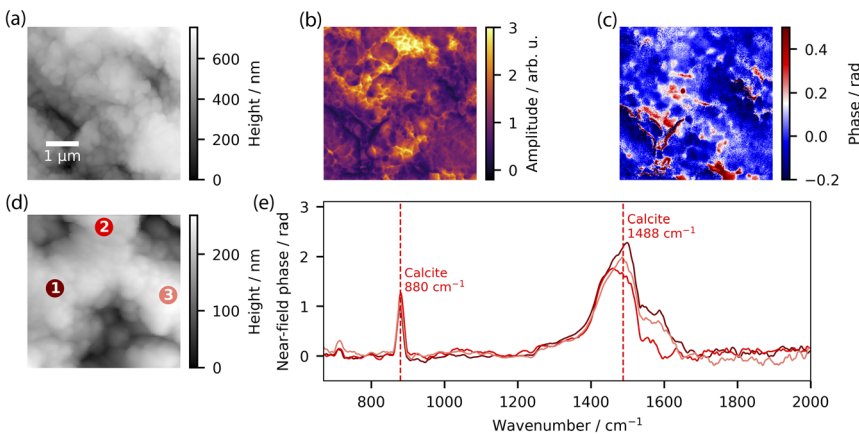


**Fig. 12** Nanoscale composition of prism layer. (a) AFM topography, (b and c) near-field amplitude and phase images at the absorption band of the organic components ( $1650\text{ cm}^{-1}$ ). Both images show an alternating structure of organic and aragonite layers. (d) and (e) AFM topography and nanoFTIR spectra. The spectra taken at different points show the characteristic calcite.



stems from an extraction procedure used to decalcify the shell. This has allowed for the determination of amino acid composition in both prisms and nacre.<sup>40,41,50</sup> Some proteins have also been identified.<sup>51,52</sup> However, proteins constitute only a portion of the organic matrix; lipids and sugars have also been described.<sup>53,54</sup>

Recently, O'Callahan *et al.*, employing a suite of nano-imaging techniques, investigated the interface between prismatic and nacreous layers in the *Pinctada margaritifera* shell.<sup>55</sup> An organic membrane separating calcite and aragonite was identified within the 910–940 cm<sup>−1</sup> spectral range, and also within the fibrous aragonite. In this article, the origin of the 910–940 cm<sup>−1</sup> spectral region remains unidentified, and no amorphous calcium carbonate was detected. Previous analyses of the soluble organic matrix extracted from the prismatic layer of *Pinctada* using HPLC and electrophoresis techniques revealed the presence of acidic and sulphated sugars.<sup>56</sup> These components have also been found in the nacreous layer of *P. fucata*.<sup>57</sup> However, the quantity of these components is low in both species, so that they are, so far, not visible in IR analyses.

## Discussion – conclusions

Our understanding of the structure, composition, and formation of biominerals remains incomplete. For example, we cannot reproduce nacre—the most well-known calcium carbonate biogenic structure—*in vitro*, due to the unique components specific to each species. These components can be categorized into two main types: the predominant 'mineral' component, examined using geological techniques, and the 'organic' component, typically analysed through biological methods. This duality—mineral and organic—introduces another distinction: observations and analyses are conducted either on the intact fragment, preserving the topographic relationships between components and avoiding alterations to the structure or composition caused by chemical treatments, or on the extracted components. Studying the extracted components, typically the organic matrix, provides access to a broader range of techniques and more detailed data. However, in this approach, the relationships between the components are disrupted.

Given these parameters, the ideal analytical system must be able to identify *in situ* the composition of the sample. Many systems are able to provide images and spectra, but most of them are dedicated to identifying mineral components or organic components.

Initially, FTIR spectroscopy was employed to characterize the mineralogy of invertebrate skeletons, primarily those of mollusks. These analyses facilitated the evaluation of diagenetic alterations to calcite and aragonite. Consequently, most spectra were acquired within the 400–1600 cm<sup>−1</sup> range, encompassing the primary vibrational bands of CaCO<sub>3</sub>. The first study of biogenic CaCO<sub>3</sub> appears to be attributed to Louisfert and Pobequin.<sup>16</sup> While they successfully identified the polymorphs, the only mention of organic components is a brief statement indicating that spectra appear "clean" when organic content is low.

In this paper, we evaluate the capabilities of various IR spectroscopy techniques using mollusk shells, for which non-IR data are available. Although these samples are produced by mollusks, their structure and composition vary. The three IR techniques employed can generate images with resolutions ranging from 5 μm to the nanoscale. Since the micro- and nanostructure has been previously



studied, SEM images help localize the IR analyses. The irregular arrangement of young pearls observed in SEM images is also visible in O-PTIR images. Additionally, the presence of lipids in *Concholepas* is confirmed. The regular structure of the nacreous layer is further evidenced by the sSNOM phase image, which detects the organic interlamellar and intercrystalline membranes.

Depending on the sample and the size of the features to be observed, SEM images enable us to select the most suitable IR techniques. The combination of SEM, potentially equipped with a microprobe, and one of the IR systems provides *in situ* data on mineral and organic materials without damaging the samples. The association of SEM-IR analytical systems is highly efficient, and moreover, the samples can be utilized for other *in situ* analyses.

## Data availability

The underlying analytical data are still being used for research and therefore, proprietary.

## Author contributions

J.-P. C. and Y. D. conceived the study. G. N. and C. S. performed the data acquisition and data analysis. C. L. provided the shells and pearls. All the other authors contributed to the interpretation of the results, the writing and the critical revision of the manuscript.

## Conflicts of interest

There are no conflicts to declare.

## Acknowledgements

This research was funded by SOLEIL synchrotron (St Aubin), grant numbers 20231339, 20221137 for SMIS beamline. Open Access funding provided by the Max Planck Society.

## References

- 1 A. van Leeuwenhoek, II. Observations upon the bones and the periosteum, in a letter to the Royal Society, from Mr. Leeuwenhoek, F. R. S., *Philos. Trans. R. Soc. London*, 1720, **31**, 91–97, DOI: [10.1098/rstl.1720.0022](https://doi.org/10.1098/rstl.1720.0022).
- 2 C. Havers, *New Observations of the Bones, and the Parts Belonging to Them, with the Manner of Their Accretion and Nutrition*, Royal Society, London, 1691, Printed for S. Smith, <https://archive.org/details/osteologianovaor0have>.
- 3 R. A. Ferchault de Réaumur, De la formation et de l'accroissement des coquilles des animaux tant terrestres qu'aquatiques, soit de mer soit de rivières, *Mém. Acad. R. Sci.*, 1709, 364400, [https://www.academiesciences.fr/pdf/dossiers/Reaumur/Reaumur\\_pdf/Hist1709\\_p17.pdf](https://www.academiesciences.fr/pdf/dossiers/Reaumur/Reaumur_pdf/Hist1709_p17.pdf).
- 4 W. B. Carpenter, On the microscopic structure of shells: part II, *Br. Assoc. Adv. Sci., Rep.*, 1847, **17**, 93–134.
- 5 E. Frémy, Recherches chimiques sur les os, *Ann. Chim. Phys.*, 1855, **43**, 47–107.

6 C. Grégoire, G. Duchateau and M. Florkin, La trame protidique des nacres et des perles, *Ann. Inst. Oceanogr.*, 1955, **31**, 1–36.

7 A. Boskey and N. P. Camacho, FT-IR imaging of native and tissue-engineered bone and cartilage, *Biomaterials*, 2007, **28**, 2465–2478.

8 O. B. Boggild, The shell structure of the molluscs, *D. Kgl. Danske Vidensk. Selsk. Skr., naturvidensk. og mathem.*, 1930, **9**(2), 231–326.

9 J. D. Taylor, W. J. Kennedy and A. Hall, The shell structure and mineralogy of the Bivalvia. I. Introduction. Nuculaceae - Trigonacae, *Bull. Br. Mus. (Nat. Hist.), Zool.*, 1969, **3**, 1–125.

10 J. D. Taylor, W. J. Kennedy and A. Hall, The shell structure and mineralogy of the Bivalvia. II. Lucinacea - Clavagellacea. Conclusions, *Bull. Br. Mus. (Nat. Hist.), Zool.*, 1973, **22**, 253–294.

11 K. Simkiss and K. Wada, Cultured pearls - commercialised biominerallisation, *Endeavour*, 1980, **4**(1), 32–37.

12 K. Wada, Formation and quality of pearls, *J. Gemmol. Soc. Jpn.*, 1999, **20**(1–4), 47–62.

13 Y. Dauphin, N. Guzman, A. Denis, J. P. Cuif and L. Ortlieb, Microstructure, nanostructure and composition of the shell of *Concholepas concholepas* (Gastropoda, Muricidae), *Aquat. Living Resour.*, 2003, **16**, 95–103.

14 N. Guzman Guerra, *Validation d'une approche scléroclimatologique sur la côte du Chili et du Pérou par l'analyse microstructurale et biogéochimique des coquilles du gastéropode Concholepas concholepas (Bruguière, 1789)*, Thèse Univ., Paris Sud, 2004.

15 L. B. Morse, The selective reflection of salts of carbonic and other oxygen acids, *Astrophys. J.*, 1907, **26**, 225–243.

16 J. Louisfert and T. Pobequin, Différenciation, au moyen des spectres d'absorption infrarouges, des carbonates de calcium, *C. R. Acad. Sci.*, 1952, **235**, 287–289.

17 C. K. Huang and P. F. Kerr, Infrared study of the carbonate minerals, *Am. Mineral.*, 1960, **45**, 311–323.

18 H. H. Adler and P. F. Kerr, Infrared study of aragonite and calcite, *Am. Mineral.*, 1962, **47**, 700–717.

19 E. L. Compere and J. M. Bates, Determination of calcite : aragonite ratios in mollusc shells by infrared spectra, *Limnol. Oceanogr.*, 1973, **18**, 326–331.

20 G. C. Jones and B. Jackson, *Infrared Transmission Spectra of Carbonate Minerals*, Chapman & Hall, London, 1993.

21 W. B. White, The carbonate minerals, in *The Infrared Spectra of Minerals*, ed. V. C. Farmer, Mineralog. Soc. monogr. 4, 1974, pp. 227–283.

22 Y. Dauphin and A. Denis, Structure and composition of the aragonitic crossed lamellar layers in six species of Bivalvia and Gastropoda, *Comp. Biochem. Physiol.*, 2000, **A126**, 367–377.

23 R. Servaty, J. Schiller, H. Binder and K. Arnold, Hydration of polymeric components of cartilage – an infrared spectroscopic study on hyaluronic acid and chondroitin sulfate, *Int. J. Biol. Macromol.*, 2001, **28**, 121e7.

24 Y. Dauphin, Infrared spectra and elemental composition in recent biogenic calcites: relationships between the v4 band wavelength and Sr and Mg concentrations, *Appl. Spectrosc.*, 1999, **53**(2), 184–190.



25 Y. Dauphin, Infrared spectra and elemental composition in recent carbonate skeletons: relationships between the v2 band wavelength and Sr and Mg concentrations, *Appl. Spectrosc.*, 1997, **51**(2), 141–152.

26 T. Moreau, J. Gautron, M. T. Hincke, P. Monget, S. Réhault-Godbert and N. Guyot, Antimicrobial proteins and peptides in avian eggshell: structural diversity and potential roles in biomineralization, *Front. Immunol.*, 2022, **13**, 946428, DOI: [10.3389/fimmu.2022.946428](https://doi.org/10.3389/fimmu.2022.946428).

27 N. Guzman, A. D. Ball, J. P. Cuif, Y. Dauphin, A. Denis and L. Ortlieb, Subdaily growth patterns and organo-mineral nanostructure of the growth layers in the calcitic prisms of the shell of *Concholepas concholepas* Bruguière, 1789 (Gastropoda, Muricidae), *Microsc. Microanal.*, 2007, **13**(5), 397–403.

28 J. P. Cuif, Données actuelles concernant la structure et la composition de la nacre et des perles, *Bull. Mus. Océanogr. Monaco, Nacres et Perles*, 1992, **8**, 77–87.

29 J. P. Cuif, Y. Dauphin, M. Gèze, C. Lo, G. Nemeth and C. Sandt, Structural diversity of the early growth stages in the Polynesian pearls reveals biological stress suffered by the grafts, *Minerals*, 2024, **14**(12), 1198, DOI: [10.3390/min14121198](https://doi.org/10.3390/min14121198).

30 J. P. Cuif, A. Perez-Huerta, C. Lo, O. Belhadj and Y. Dauphin, On the deep origin of the depressed rings on pearl surface illustrated from Polynesian *Pinctada margaritifera* (Linnaeus 1758), *Aquacult. Res.*, 2018, **49**, 1834–1847, DOI: [10.1111/are.13638](https://doi.org/10.1111/are.13638).

31 Y. Dauphin, O. Belhadj, L. Bellot-Gurlet, M. Cotte, C. Lo, K. Medjoubi, A. Somogyi, M. Salomé and J. P. Cuif, Inside black pearls, *Mater. Charact.*, 2020, **163**, 110276.

32 V. Charpentier, S. C. Phillips and S. Méry, Pearl fishing in the ancient world: 7500 BP, *Arabian Archaeol. Epigr.*, 2012, **23**, 1–6.

33 M. S. Krzemnicki, S. D. Friess, P. Chalus, H. A. Hänni and S. Karampelas, X-ray computed microtomography: distinguishing natural pearls from beaded and non-beaded culture pearls, *Gems Gemol.*, 2010, **46**, 128–134.

34 J. Rosc, V. M. F. Hammer and R. Brunner, X-ray computed tomography for fast and non-destructive multiple pearl inspection, *Case Stud. Nondestr. Test. Eval.*, 2016, **6**, 32–37.

35 V. Beltran, A. Marchetti, G. Nuyts, M. Leeuwenstein, C. Sandt, F. Borondics and K. De Wael, Nanoscale analysis of historical paintings by means of O-PTIR spectroscopy: The identification of the organic particles in L'Arlésienne (portrait of Madame Ginoux) by Van Gogh, *Angew. Chem., Int. Ed.*, 2021, **60**(42), 22753–22760.

36 I. Dev, S. Mehmood, N. Pleshko, I. Obeid and W. Querido, Assessment of submicron bone tissue composition in plastic-embedded samples using optical photothermal infrared (O-PTIR) spectral imaging and machine learning, *J. Struct. Biol.: X*, 2024, **10**, 100111.

37 S. Amarie, P. Zaslansky, Y. Kajihara, E. Griesshaber, W. W. Schmahl and F. Keilmann, Nano-FTIR chemical mapping of minerals in biological materials, *Beilstein J. Nanotechnol.*, 2012, **3**, 312–323, DOI: [10.3762/bjnano.3.35](https://doi.org/10.3762/bjnano.3.35).

38 N. Watabe and K. Wada, On the shell structures of japanese pearl oyster, *Pinctada martensii* (Dunker). (I) Prismatic layer, *Reports Fac. Fisheries, Prefec. Univ. Mie*, 1956, **2**(2), 227–231.



39 H. Nakahara and G. Bevelander, The formation and growth of the prismatic layer of *Pinctada radiata*, *Calcif. Tissue Res.*, 1971, **7**, 31–45.

40 H. Nakahara, M. Kakei and G. Bevelander, Fine structure and amino acid composition of the organic “envelope” in the prismatic layer of some bivalve shells, *Venus*, 1980, **39**(3), 167–177.

41 H. Nakahara, Nacre formation in bivalve and gastropod molluscs, in *Mechanisms and Phylogeny of Mineralization in Biological Systems*, ed. S. Suga and H. Nakahara, Springer Verlag, 1991, pp. 343–350.

42 Y. Dauphin, A. D. Ball, M. Cotte, J. P. Cuif, A. Meibom, M. Salomé, J. Susini and C. T. Williams, Structure and composition of the nacre–prisms transition in the shell of *Pinctada margaritifera* (Mollusca, Bivalvia), *Anal. Bioanal. Chem.*, 2008, **390**, 1659–1669.

43 Y. Dauphin, A. Brunelle, M. Cotte, J. P. Cuif, B. Farre, O. Laprévote, A. Meibom, M. Salomé and C. T. Williams, A layered structure in the organic envelopes of the prismatic layer of the shell of the pearl oyster *Pinctada margaritifera* (Mollusca, Bivalvia), *Microsc. Microanal.*, 2010, **16**, 91–98.

44 B. Farre, A. Brunelle, O. Laprévote, J. P. Cuif, C. T. Williams and Y. Dauphin, Shell layers of the black-lip pearl oyster *Pinctada margaritifera*: matching microstructure and composition, *Comp. Biochem. Physiol.*, 2011, **B159**(3), 131–139, DOI: [10.1016/j.cbpb.2011.03.001](https://doi.org/10.1016/j.cbpb.2011.03.001).

45 J. P. Cuif, Y. Dauphin, G. Luquet, K. Medjoubi, A. Somogyi and A. Perez-Huerta, Revisiting the organic template model through the microstructural study of shell development in *Pinctada margaritifera*, the Polynesian pearl oyster, *Minerals*, 2018, **8**, 370, DOI: [10.3390/min8090370](https://doi.org/10.3390/min8090370).

46 N. Ocelic, A. Huber and R. Hillenbrand, Pseudoheterodyne detection for background-free near-field spectroscopy, *Appl. Phys. Lett.*, 2006, **89**(10), 101124, DOI: [10.1063/1.2348781](https://doi.org/10.1063/1.2348781).

47 G. Németh, H. A. Bechtel and F. Borondics, Origins and consequences of asymmetric nano-FTIR interferograms, *Opt. Express*, 2024, **32**, 15280–15294.

48 H. Mutvei, Ultrastructural studies on cephalopod shells. Part 1: The septa and siphonal tube in *Nautilus*, *Bull. Ceol. Instn. Univ. Uppsala*, 1972, **3**, 237–261.

49 Y. Dauphin, The nanostructural unity of Mollusc shells, *Mineral. Mag.*, 2008, **72**(1), 243–246.

50 J. P. Cuif, Y. Dauphin and J. E. Sorauf, *Biominerals and Fossils through Time*, Cambridge Univ. Press, 2011.

51 C. Liu, S. Li, J. Kong, Y. Liu, W. Tianpeng and L. Xie, In-depth proteomic analysis of shell matrix proteins of *Pinctada fucata*, *Sci. Rep.*, 2015, **5**(1), 17269.

52 H. Kintsu, R. Nishimura, L. Negishi, I. Kuriyama, Y. Tsuchihashi, L. Zhu, K. Nagata and M. Suzuki, Identification of methionine-rich insoluble proteins in the shell of the pearl oyster, *Pinctada fucata*, *Sci. Rep.*, 2020, **10**(1), 18335.

53 M. Rousseau, L. Bedouet, E. Latie, P. Gasser, K. Le Ny and E. Lopez, Restoration of stratum corneum with nacre lipids, *Comp. Biochem. Physiol.*, 2006, **B145**, 1–9.

54 B. Farre and Y. Dauphin, lipids from the nacreous and prismatic layers of two Pteriomorpha Mollusc shells, *Comp. Biochem. Physiol.*, 2009, **B152**, 103–109.

55 B. T. O’Callahan, A. Larsen, S. Leichty, J. Cliff, A. C. Gagnon and M. B. Raschke, Correlative chemical and elemental nano-imaging of morphology and

disorder at the nacre-prismatic region interface in *Pinctada margaritifera*, *Sci. Rep.*, 2023, **13**, 21258, DOI: [10.1038/s41598-023-47446-5](https://doi.org/10.1038/s41598-023-47446-5).

56 Y. Dauphin, Soluble organic matrices of the calcitic prismatic shell layers of two pteriomorphid bivalves: *Pinna nobilis* and *Pinctada margaritifera*, *J. Biol. Chem.*, 2003, **278**(17), 15168–15177.

57 H. Yamagami, T. Fuji, M. Wako and Y. Hasegawa, Sulfated polysaccharide isolated from the nacre of pearl oyster improves scopolamine-induced memory impairment, *Antioxidants*, 2021, **10**, 505, DOI: [10.3390/antiox10040505](https://doi.org/10.3390/antiox10040505).

